Angle-domain common-image gathers in generalized coordinates

Jeff Shragge

ABSTRACT

The theory of angle-domain common-image gathers (ADCIGs) is extended to migrations performed in generalized 2D coordinate systems. I develop an expression linking the definition of reflection opening angle to various generalized geometric factors. I demonstrate that generalized coordinate ADCIGs can be calculated directly using Fourier-based offset-to-angle approaches for coordinate systems satisfying the Cauchy-Riemann differentiability criteria. The canonical examples of tilted Cartesian, polar, and elliptic coordinates are used to illustrate the ADCIG theory. I compare analytically and numerically generated image volumes for a set of elliptically shaped reflectors. Experiments with a synthetic data set illustrate that elliptic-coordinate ADCIGs better-resolve the reflection opening angles of steeply dipping structure, relative to conventional Cartesian image volumes, due to improved large-angle propagation and enhanced sensitivity to steep structural dips afforded by coordinate system transformations.

INTRODUCTION

Angle-domain common-image gathers (ADCIGs) are used increasingly in seismic imaging to examine migration velocity model accuracy (**?**). The key idea is that migrating with the correct velocity model leads to flat angle gathers that shift neither vertically nor horizontally as a function of reflection opening angle. Migrating with an incorrect velocity, though, leads to inconsistent angle-domain reflectivity and generates residual curvature in the ADCIG volume. ADCIGs are thus an effective velocity analysis tool and have been incorporated in wave-equation-based inversion schemes to update velocity profiles (**??**).

Wave-equation imaging techniques generate ADCIGs in straightforward manners for both shot-profile (**???**) and shot-geophone (**??**) migration approaches. In shot-profile migration, one first generates a subsurface-offset axis at each depth step by correlating the source and receiver wavefields at a number of subsurface shifts. The second step involves computing an offset-to-angle domain transformation using, for example, post-imaging Fourier-based operators (**?**).

Conventional ADCIG theory usually assumes horizontal wavefield shifts, largely because wavefield extrapolation and imaging are most commonly performed in Cartesian coordinates. However, a number of studies have noted that these ADCIG results

degrade for steeply dipping structures, such as salt flanks (**??**). Although this is partially due to problems associated with inaccurate large-angle extrapolation, ADCIGs calculated using horizontal wavefield shifts become decreasingly sensitive for increasingly steep structural dips. **?** demonstrate that this problem can be addressed by generating ADCIGs with vertical subsurface-offset-domain common-image gathers (VODCIGs); however, this approach is less desirable computationally because it requires storing the larger wavefield volumes required to calculate the VODCIGs in memory.

The introduction of shot-profile migration in more general coordinate systems [e.g. tilted Cartesian (**?**) and elliptic meshes (**?**)] presents an opportunity to circumvent problems associated with generating ADCIGs for steeply dipping structure. In particular, migration domains can be oriented such that geologic structures with steep dips in Cartesian meshes have relatively gentle dip in generalized coordinate systems, thus improving the robustness of the ADCIG calculation. Developing an ADCIG theory capable of handling more arbitrary coordinate meshes, though, requires proper treatment of the effects of non-Cartesian geometries. For example, wavefield extrapolation in non-Cartesian coordinate systems induces local wavenumber stretches, rotations and/or shearing (**?**). Similarly, non-uniform wavefield sampling can lead to anisotropic angle-domain stretching. These effects can be corrected using Jacobian change-of-variable transformations.

The goal of this paper is to extend ADCIG theory to non-Cartesian geometries. I demonstrate that ADCIG theory, as developed in a differential sense (**?**), remains valid for arbitrary geometries provided that the corresponding derivative operators are properly specified. Non-Cartesian coordinates do, however, introduce space-domain geometric factors that can render Fourier-based offset-to-angle methods unsuitable. However, I show that ADCIGs can be calculated directly in the Fourier domain for all coordinate systems satisfying the Cauchy-Riemann differentiability criteria (**?**). Moreover, ADCIGs can be calculated in all situations using the slant-stack approaches discussed in **?**.

I begin by discussing how to generate subsurface offsets and ADCIGs in Cartesian coordinates. I then provide an extension to generalized coordinate systems based on Jacobian change-of-variable arguments. I examine two canonical coordinate systems, tilted Cartesian and elliptic meshes, where the reflection angle can be explicitly calculated using Fourier-based methods, and a third, polar coordinates, where it cannot. I test the generalized ADCIG theory analytically and numerically using a set of elliptic reflectors, and demonstrate how computing angle gathers in elliptic coordinates can lead to improvements relative to Cartesian coordinates, especially for steeply dipping structure.

ADCIG THEORY

The ADCIG theory presented in this section draws from that presented in **?**. In the ensuing development, $\boldsymbol{x} = [x_1, x_3]$ denotes the Cartesian variables and $\boldsymbol{\xi} = [\xi_1, \xi_3]$ represents a generalized Riemannian coordinate system. I also use a convention where the extrapolation axis is oriented in the x_3 (ξ_3) direction for Cartesian (Riemannian) coordinates. Coordinates $x_2 = \xi_2 = 0$ are assumed throughout.

Generating subsurface offsets axes

Shot-profile migration in Cartesian coordinates consists of completing a recursive two-step procedure. The first step involves propagating the source and receiver wavefields, S and R, from depth level $x_3 - \Delta x_3$ to x_3 using an extrapolation operator $E_{x_3}[\cdot]$

$$\begin{aligned} E_{x_3}[S(x_3 - \Delta x_3, x_1|\omega)] &= S(x_3, x_1|\omega), \\ E^*_{x_3}[R(x_3 - \Delta x_3, x_1|\omega)] &= R(x_3, x_1|\omega), \end{aligned} \tag{1}$$

where $*$ denotes the conjugate operator, ω is angular frequency, and Δx_3 is the depth step. A subsurface image, I, is subsequently computed at each extrapolation step by evaluating an imaging condition

$$I(x_3, x_1, h_{x_1}) = \sum_{\omega} S^*(x_3, x_1 - h_{x_1}|\omega) R(x_3, x_1 + h_{x_1}|\omega), \tag{2}$$

where the subsurface-offset axis, h_{x_1}, is generated by correlating the source and receiver wavefields at various relative shifts in the x_1 direction. Finally, the ADCIG volume is computed using an offset-to-angle transformation operator, $\mathbf{T}_{h_{x_1} \rightarrow \gamma}$

$$I(x_3, x_1, \gamma) = \mathbf{T}_{h_{x_1} \rightarrow \gamma} I(x_3, x_1, h_{x_1}), \tag{3}$$

where γ is the reflection opening angle shown in Figure 1.

Imaging in generalized coordinate systems follows the same two-step procedure. However, because of the different migration geometry in the $\boldsymbol{\xi}$-coordinate system, new extrapolation operators, $E_{\xi_3}[\cdot]$, must be used to propagate wavefields. I specify these operators using Riemannian wavefield extrapolation (RWE). I do not discuss RWE herein, and refer readers interested in additional information to **?** and **?**.

The first generalized coordinate imaging step is performing wavefield extrapolation

$$\begin{aligned} E_{\xi_3}[S(\xi_3 - \Delta\xi_3, \xi_1|\omega)] &= S(\xi_3, \xi_1|\omega), \\ E^*_{\xi_3}[R(\xi_3 - \Delta\xi_3, \xi_1|\omega)] &= R(\xi_3, \xi_1|\omega), \end{aligned} \tag{4}$$

where $\Delta\xi_3$ is the extrapolation step increment. Generalized coordinate images are then constructed by evaluating an imaging condition

$$I(\xi_3, \xi_1, h_{\xi_1}) = \sum_{\omega} S^*(\xi_3, \xi_1 + h_{\xi_1}|\omega) R(\xi_3, \xi_1 - h_{\xi_1}|\omega), \tag{5}$$

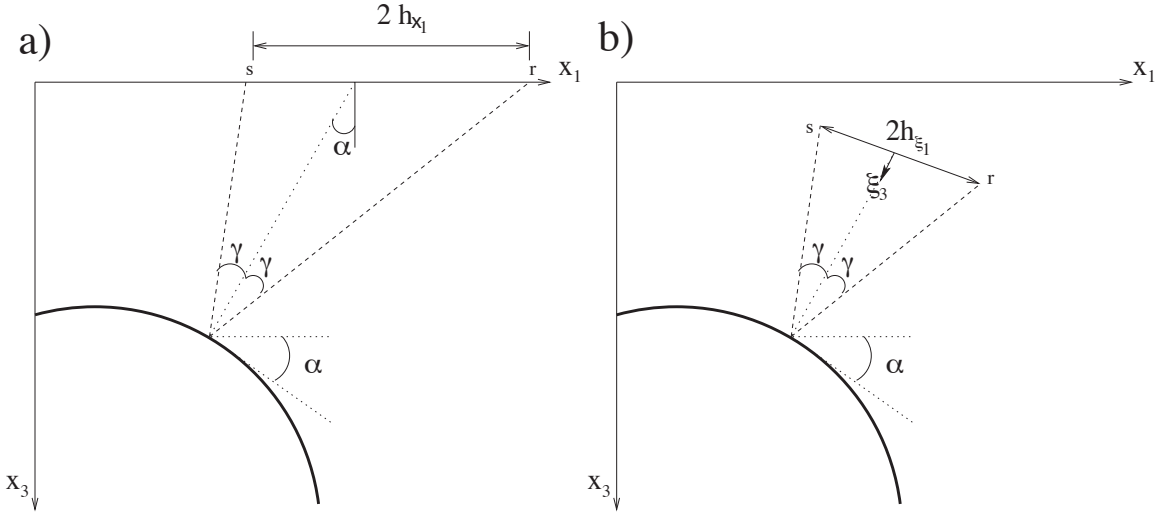

Figure 1: Cartoon illustrating the geometry of the ADCIG calculation. Parameter γ is the reflection opening angle, α is geologic dip. a) Cartesian geometry using coordinates x_1, x_3 andh_{x_1}. b) Generalized geometry using coordinates ξ_1, ξ_3 and h_{ξ_1}. Adapted from **?**.

where h_{ξ_1} is the $\boldsymbol{\xi}$-coordinate equivalent of Cartesian subsurface offset axis h_{ξ_1}. The generalized coordinate ADCIG volume is generated by applying an offset-to-angle transformation $\mathbf{T}_{h_\xi \rightarrow \gamma}$

$$I(\xi_3, \xi_1, \gamma) = \mathbf{T}_{h_{\xi_1} \rightarrow \gamma} I(\xi_3, \xi_1, h_{\xi_1}). \tag{6}$$

Conventional ADCIG volumes can be recovered by sinc interpolating each $I(\xi_3, \xi_1, \gamma)$ image computed via equation 6 to the final Cartesian coordinate volume.

Figure 2 illustrates this process using the elliptic coordinate system. Panel 2a shows the BP synthetic velocity model (**?**) with an elliptic mesh overlain. Note that the salt flanks to the right-side of the model are nearly vertical in Cartesian coordinates. Panel 2b shows the velocity model in panel 2a interpolated to the elliptic coordinate system. Importantly, the aforementioned salt flanks in the elliptic coordinate system are nearly horizontal, which should lead to ADCIG calculations more robust than in Cartesian coordinates. However, proving this assertion requires understanding the differences, if any, between the Cartesian and generalized coordinate offset-to-angle operators, $\mathbf{T}_{h_{x_1} \rightarrow \gamma}$ and $\mathbf{T}_{h_{\xi_1} \rightarrow \gamma}$, in equations 3 and 6, respectively.

Cartesian coordinate ADCIGs

For constant velocity media in conventional Cartesian geometry, a straightforward link exists between differential changes in the travel time, t, of rays connecting the source-reflector and reflector-receiver paths to changes in the subsurface offset, h_{x_1}, and depth, x_3, coordinates. Figure 1a shows the geometry of these variables.

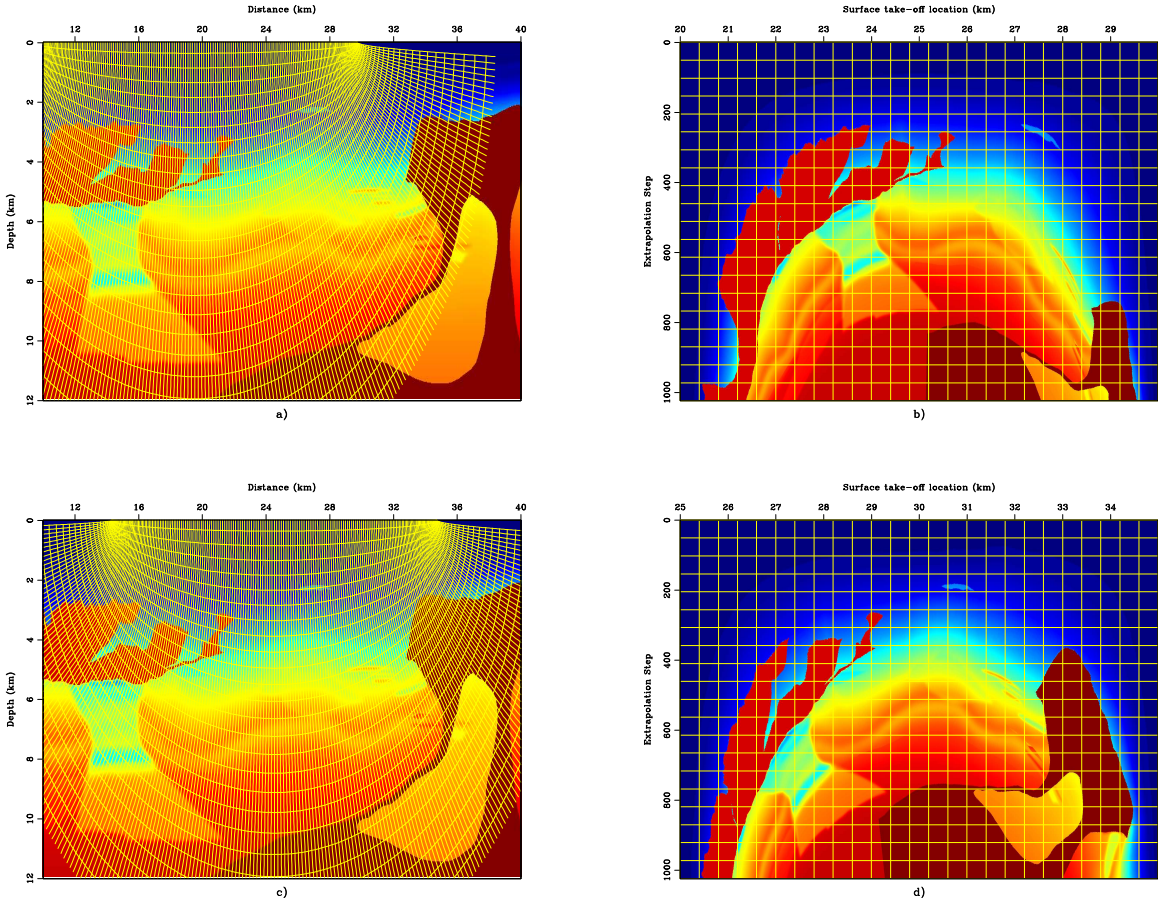

Figure 2: Prestack migration test in elliptic coordinates. a) Benchmark synthetic velocity model with an overlying elliptic coordinate system. b) Effective slowness model in the transformed elliptic coordinate system in a). c) Benchmark synthetic velocity model with a different overlying elliptic coordinate system. d) Effective elliptic coordinate slowness model for the coordinate system in c).

Mathematically, these relationships are

$$\begin{bmatrix} \frac{\partial t}{\partial h_{x_1}} \\ \frac{\partial t}{\partial x_3} \end{bmatrix} = 2\, s \cos\alpha \begin{bmatrix} \sin\gamma \\ \cos\gamma \end{bmatrix}, \tag{7}$$

where s is slowness, α is reflector dip, and γ is the reflection opening angle. The right-hand-side of equations 7 are derived by **?**. Equations 7 can be rewritten as

$$-\left.\frac{\partial x_3}{\partial h_{x_1}}\right|_{x_1,t} = \frac{\partial t}{\partial h_{x_1}} \Big/ \frac{\partial t}{\partial x_3} = \tan\gamma, \tag{8}$$

where the negative sign derives from use of the implicit functions theory (**?**). **?** note that Cartesian ADCIGs become pathogenically degenerate in situations where $\frac{\partial t}{\partial x_3} \rightarrow 0$ (i.e. for steeply dipping structures where $\alpha \rightarrow 90^\circ$ in Figure 1). However, vertically oriented structures are, generally, not well imaged in Cartesian coordinates because of limited steep-angle propagation in downward extrapolation.

Finally, because equation 7 has no explicit geometric-dependence, Fourier-based methods can calculate the reflection opening angle directly in the wavenumber domain

$$\tan\gamma = -\frac{k_{h_{x_1}}}{k_{x_3}}, \tag{9}$$

where $k_{h_{x_1}}$ and k_{x_3} are the wavenumbers in the h_{x_1} and x_3 directions, respectively.

Generalized coordinate ADCIGs

Figure 1b illustrates a scenario similar to that in Figure 1a, but for a more general coordinate system. The reflection opening angle, γ, and the reflector dip, α, obviously remain unchanged in the subsurface; however, the orientations of the h_{ξ_1} and ξ_3 axes used to estimate γ now differ. The key question is, which quantities in the ADCIG calculation are affected by this change of variables?

Answering this question requires properly formulating the derivative operators, $\frac{\partial}{\partial x_3}$ and $\frac{\partial}{\partial h_{x_1}}$, in equations 7 in the generalized coordinate system variables $\boldsymbol{\xi} = [\xi_1, \xi_3]$ and $\boldsymbol{h_\xi} = [h_{\xi_1}, h_{\xi_3}]$. Appendix A shows how these derivatives can be specified using Jacobian change-of-variable arguments. Assuming that the subsurface-offset axes are formed by uniform wavefield shifts, Appendix A derives the following expression for generalized coordinate ADCIGs:

$$-\left.\frac{\partial \xi_3}{\partial h_{\xi_1}}\right|_{\xi_1,t} = \frac{\partial t}{\partial h_{\xi_1}} \Big/ \frac{\partial t}{\partial \xi_3} = \tan\gamma\, \frac{\left(\frac{\partial x_1}{\partial \xi_1}\cos\alpha - \frac{\partial x_3}{\partial \xi_1}\sin\alpha\right)}{\left(\frac{\partial x_3}{\partial \xi_3}\cos\alpha + \frac{\partial x_1}{\partial \xi_3}\sin\alpha\right)}. \tag{10}$$

Note that if the $\boldsymbol{\xi}$-coordinate system satisfies the Cauchy-Riemann differentiability criteria (**?**)

$$\frac{\partial x_1}{\partial \xi_1} = \frac{\partial x_3}{\partial \xi_3} \quad \text{and} \quad \frac{\partial x_3}{\partial \xi_1} = -\frac{\partial x_1}{\partial \xi_3}, \tag{11}$$

equation 10 then reduces to

$$-\left.\frac{\partial \xi_3}{\partial h_{\xi_1}}\right|_{\xi_1,t} = \tan\gamma. \tag{12}$$

This is the generalized coordinate equivalent of the Cartesian expression in equation 7. A physical meaning of the criteria in equations 11 is that the coordinate system must behave isotropically (i.e. dilatationally and rotationally) in the neighborhood of every grid point. Three canonical examples, two of which satisfy equations 11, are discussed in the following section.

Similar to Cartesian coordinates, elliptic coordinate ADCIGs become insensitive where structural dips cause $\frac{\partial t}{\partial \xi_3} \rightarrow 0$. However, this insensitivity can be minimized when using generalized coordinate systems, because structural dips appear at different angles in different translated elliptic meshes. Figures 2c-d illustrate this by showing a different coordinate shift for a different shot-location than that presented in panels 2a-b. Note the changes in structural dip in the right-hand-side of the elliptic coordinate panels. Thus, while ADCIGs calculated on one elliptic grid may be insensitive to certain structure locally, mesh translation ensures that ADCIGs are sensitive globally. Imaging steep dips in elliptic coordinates, though, is limited by the accuracy of wide-angle one-way wavefield extrapolation.

Finally, one may calculate reflection opening angles in the wavenumber domain for coordinate systems satisfying equations 11

$$\tan\gamma = -\frac{k_{h_{\xi_1}}}{k_{\xi_3}}, \tag{13}$$

where $k_{h_{\xi_1}}$ and k_{ξ_3} are the wavenumbers in the h_{ξ_1} and ξ_3 directions, respectively. While some non-orthogonal coordinate systems might satisfy equations 11, most practical applications will have orthogonal $k_{h_{\xi_1}}$ and k_{ξ_3}.

CANONICAL EXAMPLES

This section presents three canonical examples that illustrate the generalized ADCIG theory: tilted Cartesian, polar, and elliptic coordinate systems. Figure 3 presents schematic examples of these three coordinate systems.

Tilted Cartesian coordinates

Tilted Cartesian coordinates are a useful generalized migration coordinate system (see Figure 3a). **?** use this mesh in a plane-wave migration scheme where the coordinate system is oriented toward the plane-wave take-off angle to improve large-angle propagation accuracy. A tilted Cartesian mesh is defined by

$$\begin{bmatrix} x_1 \\ x_3 \end{bmatrix} = \begin{bmatrix} \cos\theta & -\sin\theta \\ \sin\theta & \cos\theta \end{bmatrix} \begin{bmatrix} \xi_1 \\ \xi_3 \end{bmatrix}, \tag{14}$$

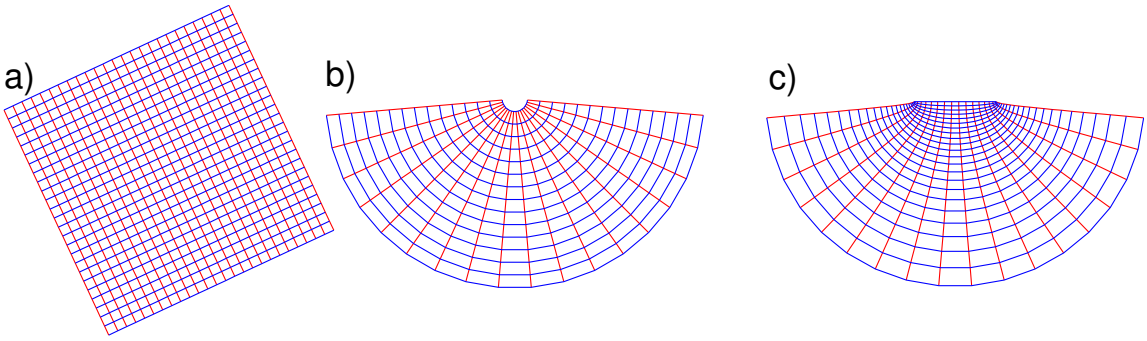

Figure 3: Canonical coordinate system examples. a) Tilted Cartesian coordinates. b) Polar coordinates. c) Elliptic coordinates.

where θ is the tilt angle. The partial derivative transform matrix is

$$\begin{bmatrix} \frac{\partial x_1}{\partial \xi_1} & \frac{\partial x_1}{\partial \xi_3} \\ \frac{\partial x_3}{\partial \xi_1} & \frac{\partial x_3}{\partial \xi_3} \end{bmatrix} = \begin{bmatrix} \cos\theta & -\sin\theta \\ \sin\theta & \cos\theta \end{bmatrix}, \tag{15}$$

which leads to the following ADCIG equation:

$$-\left.\frac{\partial \xi_3}{\partial h_{\xi_1}}\right|_{\xi_1,t} = \tan\gamma \, \frac{(\cos\theta\cos\alpha + \sin\theta\sin\alpha)}{(\cos\theta\cos\alpha + \sin\theta\sin\alpha)} = \tan\gamma. \tag{16}$$

Thus, calculating ADCIGs in tilted Cartesian coordinates directly recovers the correct reflection opening angle. Note that setting $\theta = 0^\circ$ recovers the Cartesian expression in equation 8.

Polar coordinates

The polar coordinate system (see Figure 3b), where the extrapolation direction is oriented along the radial direction, is appropriate for generating 2D Green's function estimates. The polar coordinate system is defined by

$$\begin{bmatrix} x_1 \\ x_3 \end{bmatrix} = \begin{bmatrix} a\,\xi_3\cos\xi_1 \\ a\,\xi_3\sin\xi_1 \end{bmatrix}. \tag{17}$$

The partial derivative transformation matrix is

$$\begin{bmatrix} \frac{\partial x_1}{\partial \xi_1} & \frac{\partial x_1}{\partial \xi_3} \\ \frac{\partial x_3}{\partial \xi_1} & \frac{\partial x_3}{\partial \xi_3} \end{bmatrix} = \begin{bmatrix} -a\,\xi_3\sin\xi_1 & a\cos\xi_1 \\ a\,\xi_3\cos\xi_1 & a\sin\xi_1 \end{bmatrix}, \tag{18}$$

which leads to the following ADCIG equation:

$$-\left.\frac{\partial \xi_3}{\partial h_{\xi_1}}\right|_{\xi_1,t} = \xi_3\tan\gamma \, \frac{(-\sin\xi_1\cos\alpha - \cos\xi_1\sin\alpha)}{(\sin\xi_1\cos\alpha + \cos\xi_1\sin,\alpha)} = -\xi_3\tan\gamma. \tag{19}$$

Thus, one cannot calculate ADCIGs directly with Fourier-based methods in polar coordinates because of the spatial geometric dependence on ξ_3. However, polar-coordinate ADCIGs can be calculated using slant-stack operators (**?**), because the geometric factor ξ_3 is no more than a local weight applied to the velocity model used to calculate the angle gathers.

Elliptic coordinates

Elliptic coordinates (see Figure 3c) are a useful coordinate system for performing 2D shot-profile migration (**?**). An elliptic mesh is defined by

$$\begin{bmatrix} x_1 \\ x_3 \end{bmatrix} = \begin{bmatrix} a\cosh\xi_3\cos\xi_1 \\ a\sinh\xi_3\sin\xi_1 \end{bmatrix}. \tag{20}$$

The partial derivative transformation matrix is

$$\begin{bmatrix} \frac{\partial x_1}{\partial \xi_1} & \frac{\partial x_1}{\partial \xi_3} \\ \frac{\partial x_3}{\partial \xi_1} & \frac{\partial x_3}{\partial \xi_3} \end{bmatrix} = a \begin{bmatrix} \cosh\xi_3\sin\xi_1 & \sinh\xi_3\cos\xi_1 \\ -\sinh\xi_3\cos\xi_1 & \cosh\xi_3\sin\xi_1 \end{bmatrix}, \tag{21}$$

which leads to the following ADCIG equation:

$$-\left.\frac{\partial \xi_3}{\partial h_{\xi_1}}\right|_{\xi_1,t} = \tan\gamma\,\frac{(\cosh\xi_3\sin\xi_1\cos\alpha - \sinh\xi_3\cos\xi_1\sin\alpha)}{(\cosh\xi_3\sin\xi_1\cos\alpha - \sinh\xi_3\cos\xi_1\sin\alpha)} = \tan\gamma. \tag{22}$$

Thus, calculating ADCIGs in elliptic coordinates with Fourier-based methods will directly recover the true reflection opening angle.

NUMERICAL EXAMPLES

This section presents numerical tests of the generalized theory by comparing the ADCIG volumes for elliptic and Cartesian coordinate systems. I generated the results using a shot-profile migration algorithm altered to account for elliptic geometry by replacing the Cartesian extrapolator, $E_{x_3}[\cdot]$, with an elliptic coordinate operator, $E_{\xi_3}[\cdot]$. In both coordinate systems, the implemented extrapolation operators were accurate to roughly 80° (Lee and Suh, 1985) with respect to the extrapolation axis. The reader is referred to **?** for further implementation details on shot-profile migration in elliptic coordinates.

I calculated ADCIG image volumes for each shot-profile by following a three-step procedure: 1) generate image volume $I(\xi_1, \xi_3, h_{\xi_1})$ by computing the image for 64 subsurface shifts in h_{ξ_1} at each point in every extrapolation step; 2) calculate ADCIG volume $I(\xi_1, \xi_3, \gamma)$ using the procedure described in **?**; and 3) output the image $I(x_1, x_3, \gamma)$ by sinc-based interpolation of single-shot ADCIGs to the global volume. Steps 1-3 were repeated for all shot-profile sections contributing to the final image.

Test 1: Elliptic Isochrons

The first test demonstrates the impulse response of the ADCIG imaging operator. I do this by imaging the elliptic isochronal responses of two offset point sources in a constant velocity medium (see Figure 4). The source wavefield impulse is at time $t = 0$ s and at $x = -1.12$ km, while the receiver wavefield impulses are at $t = 2.0$, 2.5, 3.0, and 3.5 s and $x = 1.12$ km for a total source-receiver offset of $2h = 2.24$ km. Correlating these two wavefield volumes leads to four elliptic isochrons specified by

$$x_1(t,h) = \frac{vt}{4}\left(\cos\theta_1 + \cos\theta_2\right) \tag{23}$$

$$x_3(t,h) = \frac{vt}{4}\left(1 - \frac{h^2}{v^2t^2}\right)\left(\sin\theta_1 + \sin\theta_2\right), \tag{24}$$

where, given the source take-off angle θ_1, the receiver take-off angle θ_2 is obtained by

$$\theta_2 = \cos^{-1}\left(\frac{vt}{2h}\left[\frac{1}{\frac{2}{1-\frac{4h^2}{v^2t^2}} - \frac{1}{1-\frac{2h\cos\theta_1}{vt}}} - 1\right]\right). \tag{25}$$

The reflection opening angle, given by $\gamma = 90 - \frac{(\theta_1+\theta_2)}{2}$, is shown color-coded on the scatterplot in Figure 4.

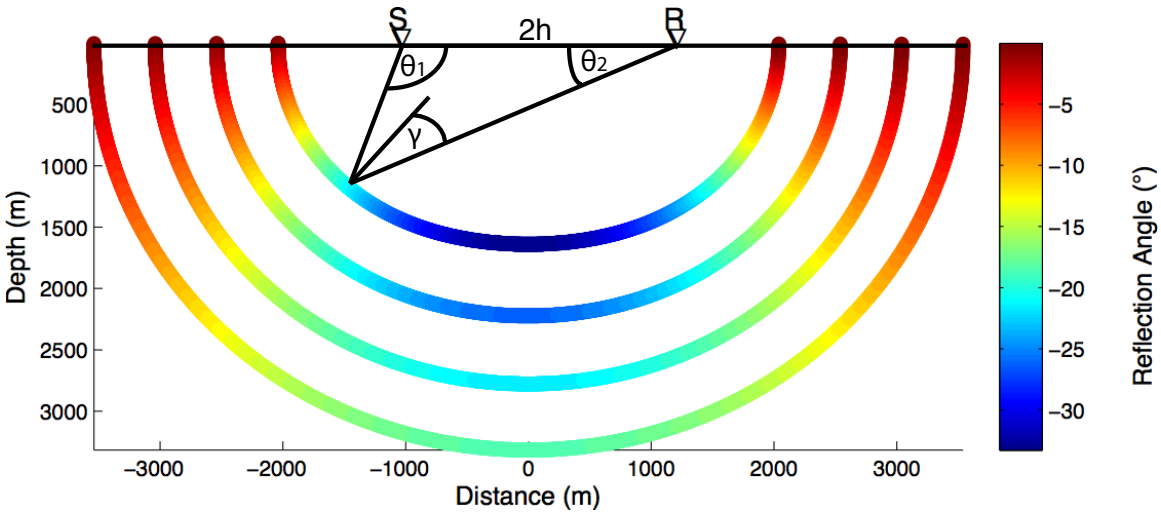

Figure 4: Theoretical results for an elliptic isochron for four travel times in a constant velocity medium. The elliptic surfaces are color-coded according to reflection opening angle.

Figure 5 shows the ADCIG volumes calculated in both (a single) elliptic and Cartesian coordinate system. To generate this image, I first calculated an elliptic coordinate (EC) volume $I(\xi_1, \xi_3, h_{\xi_1})$ by correlating the source and receiver wavefields at 64 subsurface shifts in h_{ξ_1} at each point in every extrapolation step. I then input the

ODCIG volume to a Fourier-based offset-to-angle transformation operator to generate the EC ADCIG volume, $I(\xi_1, \xi_3, \gamma)$, which I interpolated to Cartesian coordinates to generate the desired image volume, $I(x_1, x_3, \gamma)$. For the ADCIG transformation, I choose to limit the maximum opening angle to $\gamma = \pm 60°$. Thus, the 64 image shifts lead to ADCIGs with an angular range between $-60° < \gamma < 60°$ with a sampling increment of $\Delta\gamma = 1.875°$.

Panel 5a presents the elliptic coordinate image extracted at $\gamma = -24°$ from the ADCIG volume $I(x_1, x_3, \gamma)$. The ADCIG volumes consist of elliptically shaped reflectors (panels 5a) that are ideally localized in the angle domain (panels 5b-c and f-h). The analytical ADCIG locations are represented by black dots. The analytically and numerically generated results are well matched. Figure 5a also shows three vertical lines indicating the locations from left to right of the three ADCIGs in panels 5b-d. Again, the analytic and numerical ADCIGs are well matched, though less so at shallower depths due to the increased smearing about the image point in the $I(\xi_1, \xi_3, h_{\xi_1})$ domain (**?**).

The Cartesian coordinate (CC) ADCIGs are presented in panels 5e-h. Panel 5e shows the Cartesian image again extracted at $\gamma = -24°$ in the angle domain. Panels 5f-h present three ADCIGs at the same locations as in panels 5b-d. The Cartesian image volumes are well-matched to the elliptic coordinate examples, and good agreement between the theoretical results and the wavefield volume is observed in both images. Energy is focused in the neighborhood of the correct locations. The angle gathers are not always centered relative to the true location, though, which is more noticeable at shallower depths where the Cartesian and elliptic ADCIG volumes both overestimate the reflection opening angle.

Figure 6 presents the results of a test similar to that shown in Figure 5, but with the velocity model rescaled by 0.98. Again, the black dots show the location of the true image point (assuming a true velocity model). Note that the image points in each ADCIG remain well-focused, but shift nearer to the surface and to wider angles. Thus, imaging with an overly slow velocity model will generate, as expected, reflectors that exhibit upward curvature at wider angles.

Test 2: BP velocity model

The second test compares elliptic and Cartesian coordinate ADCIG volumes computed for the BP synthetic velocity model. Images computed in elliptic coordinates used only one coordinate system per shot. For the one-sided data set, I used a (surface) migration aperture of 12km and located the source and farthest offset receiver (at 8km) points 2km in from the edges of the computational mesh. (Note that the migration aperture effectively expands during wavefield extrapolation because the coordinate mesh expands outward.) I found this initial migration geometry to produce the best results for the BP synthetic model through iterative testing. Generally, the optimal elliptic coordinate migration geometry is controlled by the velocity model.

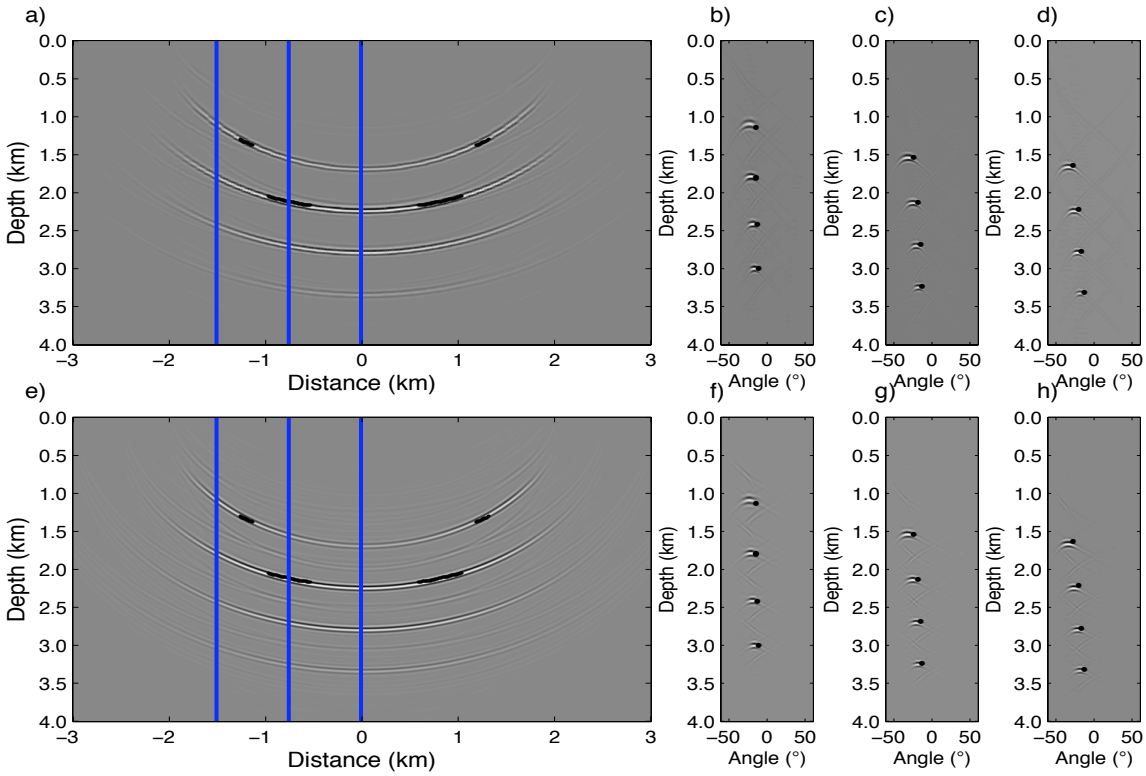

Figure 5: Elliptic reflector comparison tests between analytically (black bullets) and numerically generated ADCIG volumes. Panels a-d are computed in elliptic coordinates (EC), while panels e-h are in Cartesian coordinates (CC). a) EC image extracted at the -24° reflection angle. b) EC angle gather at -1.5 km. c) EC gather at 0.75 km. d) EC gather at 0.0 km. e) CC image extracted at the -24° reflection angle. f) CC angle gather at -1.5 km. g) CC gather at 0.75 km. h) CC gather at 0.0 km.

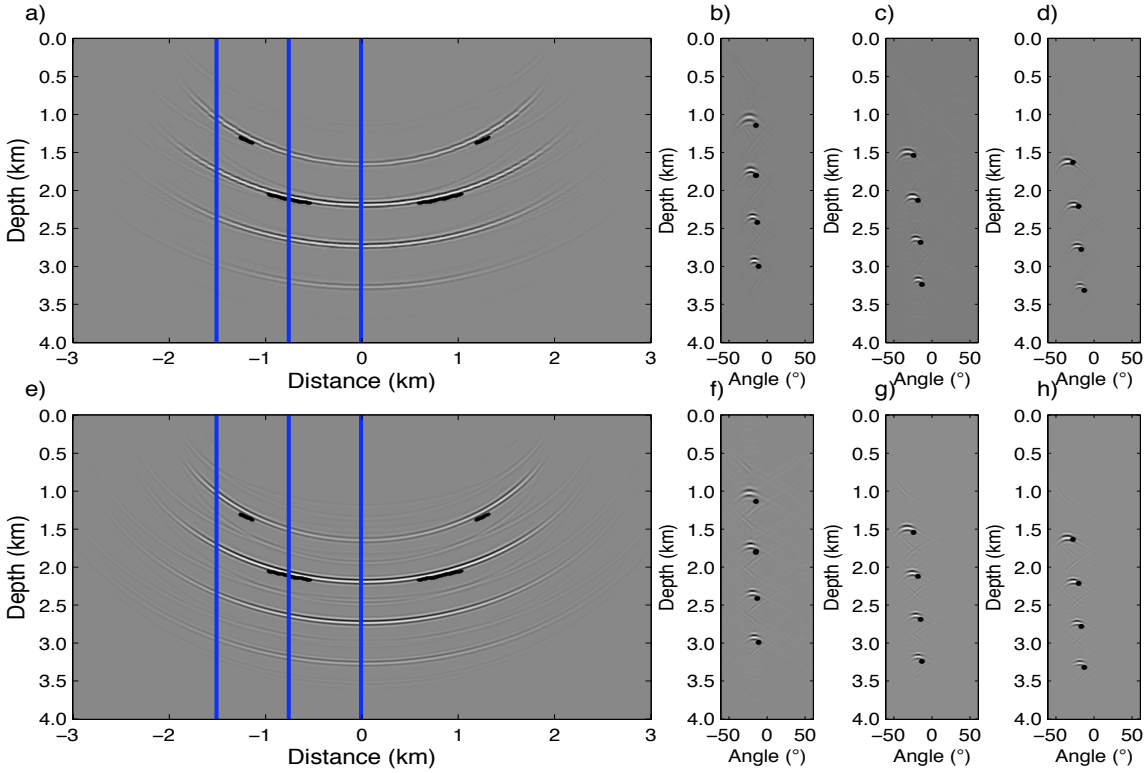

Figure 6: Elliptic reflector comparison tests between analytically (black bullets) and numerically generated ADCIG volumes using a velocity scaled by factor 0.98. Panels a-d are computed in elliptic coordinates (EC), while panels e-h are in Cartesian coordinates (CC). a) EC image extracted at the -24° reflection angle. b) EC angle gather at -1.5 km. c) EC gather at 0.75 km. d) EC gather at 0.0 km. e) CC image extracted at the -24° reflection angle. f) CC angle gather at -1.5 km. g) CC gather at 0.75 km. h) CC gather at 0.0 km.

Figure 7 shows slices all clipped at the 99^{th} percentile from the corresponding elliptic and Cartesian ADCIG image volumes. Panel 7a shows an elliptic coordinate

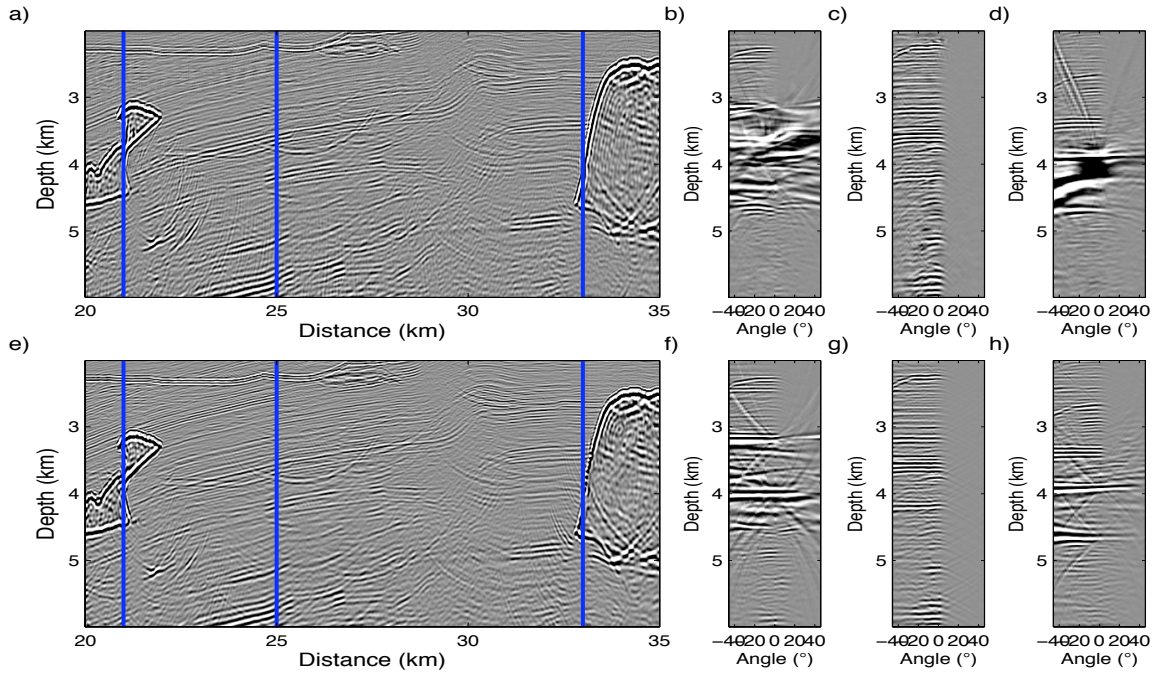

Figure 7: Vertical elliptic and Cartesian ADCIGs slices using the correct migration velocity model. a) Elliptic coordinate image with three vertical lines showing the locations of ADCIG gathers from left to right in panels b-d. e) Cartesian coordinate image with three vertical lines showing the locations of ADCIG gathers from left to right in panels f-h.

image with three vertical lines indicating the angle-gather locations from left to right in Figures 7b-d. The three panels show predominantly one-sided reflectivity, which is to be expected because the input migration data were not in a split-spread geometry. (This statement holds for all subsequent images calculated using this data set.) The only significant exceptions occur in panel 7b within salt where energy is exhibited for both positive and negative reflection angles. I attribute this to the reversal of source and receiver wavefield orientations within the salt.

The image in panel 7d has a wide reflection zone between 3.75-4.25 km in depth, which occurs because the shown angle gather is a vertical slice through the nearly vertical salt flank. This creates the appears of low-frequency noise, which is the appropriate response for a near-vertical reflector. Panel 7e shows the Cartesian image for the same location as panel 7a, while panels 7f-h are extracted from the same locations as panels 7b-d. The Cartesian angle gathers look similar to those in elliptic coordinates, except for the salt flanks to the right-hand-side of panel 7h.

A final observation from Figure 7 is that ADCIGs calculated via subsurface correlations will generate artifacts at locations near salt-sediment interfaces - whether in an elliptic or a Cartesian coordinate system. This geologic setting leads to situa-

tions where a wavefield sample inside a salt body is correlated with another sample located in the sediment with a significantly different velocity. This velocity difference violates one of the theoretical ADCIG assumptions, namely that the velocity remains constant across the correlation window. Hence, one must be careful not to interpret ADCIG artifacts as signal useful for migration velocity analysis.

Figure 8 shows horizontal slices that better resolve the vertical salt flank. Panel 8a presents the elliptic coordinate image, with three horizontal lines showing the ADCIG slice locations from top to bottom. The right-hand sides of panels 8b-d display the well-focused vertical salt-flank reflector. This demonstrates the robustness of the ADCIG calculation in elliptic coordinates. Panel 8e shows the Cartesian coordinate image with three horizontal lines showing the locations of the ADCIG slices. The right-hand salt-flank reflector in panel 8f is similarly well-resolved, largely because the structural dip is relatively low. However, the salt-flank images in panels 8g-h are somewhat blurred out. I attribute this to the combined effects of inaccurate large-angle extrapolation and insensitivity of the ADCIG calculation to steep structural dip.

An additional test examines how the ADCIG volumes change when introducing an incorrect migration velocity profile. Figure 9 presents ADCIG volumes similar to those shown in Figure 7 after using a migration velocity profile rescaled by 98%. Both images are poorly focused and have residual curvature indicating an incorrect migration velocity. Because the reflectors are near vertical, though, the sensitivity of horizontal gathers is weak. This low sensitivity is greatly improved when examining the horizontal slices in Figure 10 taken at the same locations as in Figure 8. The elliptic angle gathers in panels 10b-d, and especially to the right-hand side in panel 10d, show much greater residual curvature. This indicates that the elliptic coordinate horizontal ADCIGs have greater sensitivity to velocity error for near-vertical structures than Cartesian coordinate horizontal ADCIGs. The imaging enhancements afforded by elliptic coordinates should improve any migration velocity analysis approach that uses residual curvature in steeply dipping reflectors to compute velocity model updates.

Discussion

Extending the above theory of generalized coordinate ADCIGs to 3D coordinate systems is fairly straightforward, though more difficult to implement numerically. **?** presents a theory for 3D Cartesian coordinates that specifies the differential traveltime expressions required to express the reflection opening angle, γ, in 3D Cartesian ADCIGs [see equation 16 in **?**]. Applying Jacobian change-of-variable transformations to these equations should yield a 3D expression for reflection angle. Similar to 3D Cartesian coordinates, though, this quantity will depend on geologic dips and need to be computed by one of the two algorithms suggested by **?**.

Given that a 3D expression can be formulated, there are a number of coordinate

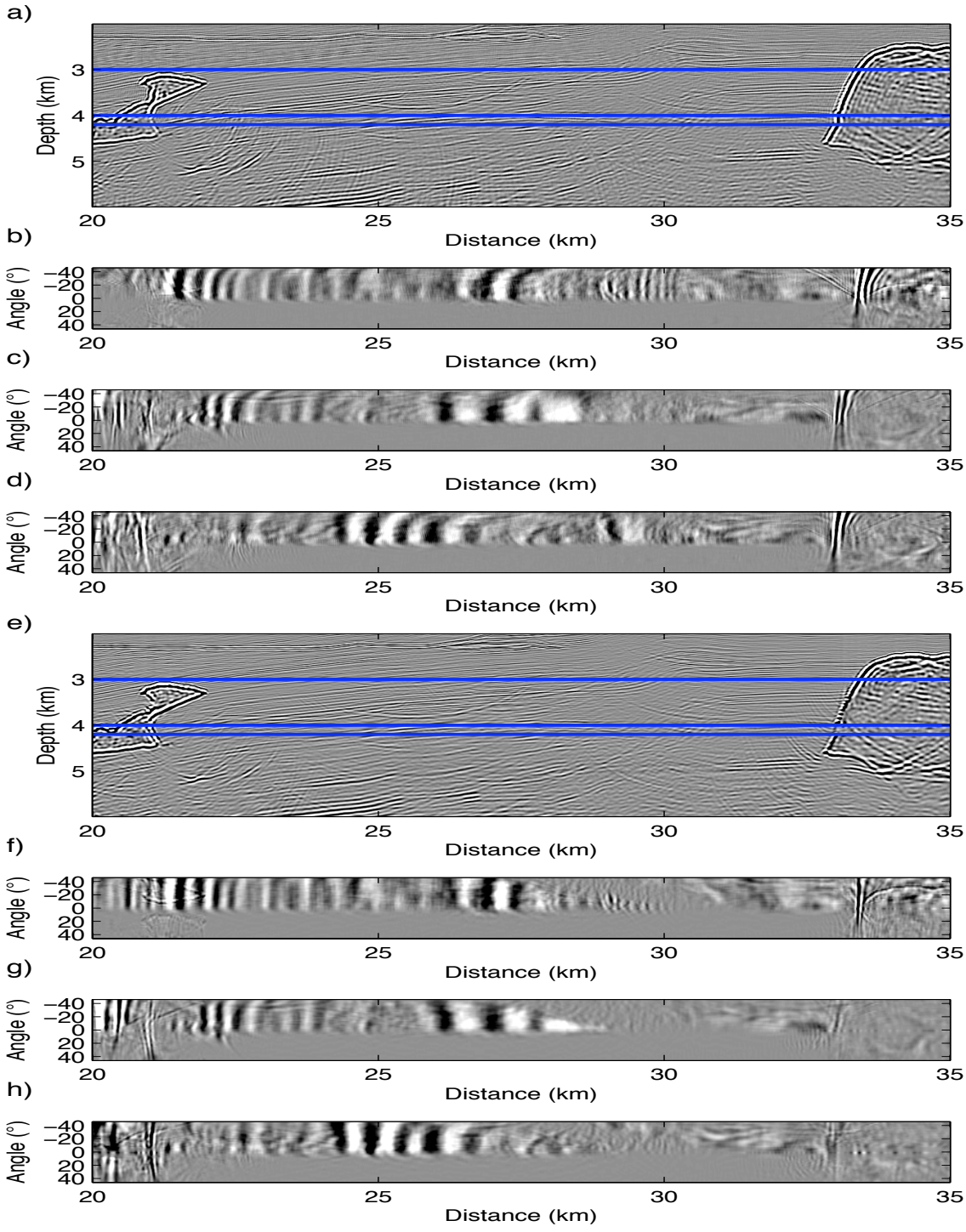

Figure 8: Horizontal elliptic and Cartesian ADCIGs slices using the correct migration velocity model. a) Elliptic coordinate image with three horizontal lines showing the locations of horizontal ADCIG gathers from top to bottom in panels b-d. e) Cartesian coordinate image with three horizontal lines showing the locations of horizontal ADCIG gathers from top to bottom in panels f-h.

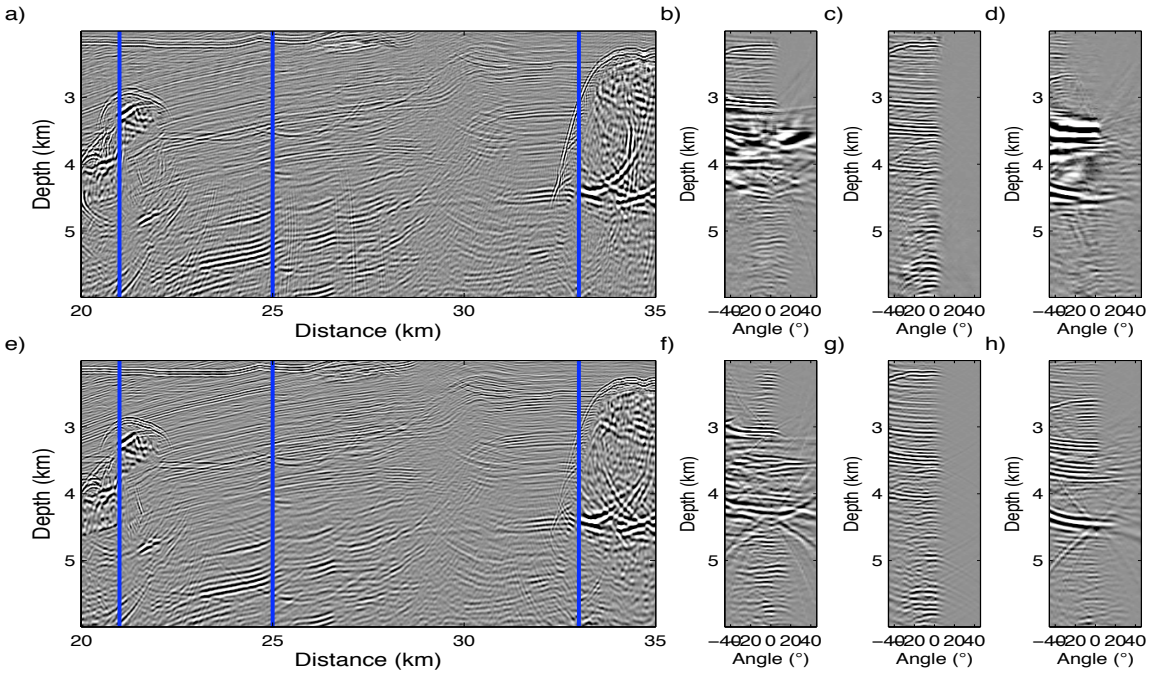

Figure 9: Vertical elliptic and Cartesian ADCIGs slices using an incorrect migration velocity model. a) Elliptic coordinate image with three vertical lines showing the locations of vertical ADCIG gathers from left to right in panels b-d. e) Cartesian coordinate image with three vertical lines showing the locations of vertical ADCIG gathers from left to right in panels f-h.

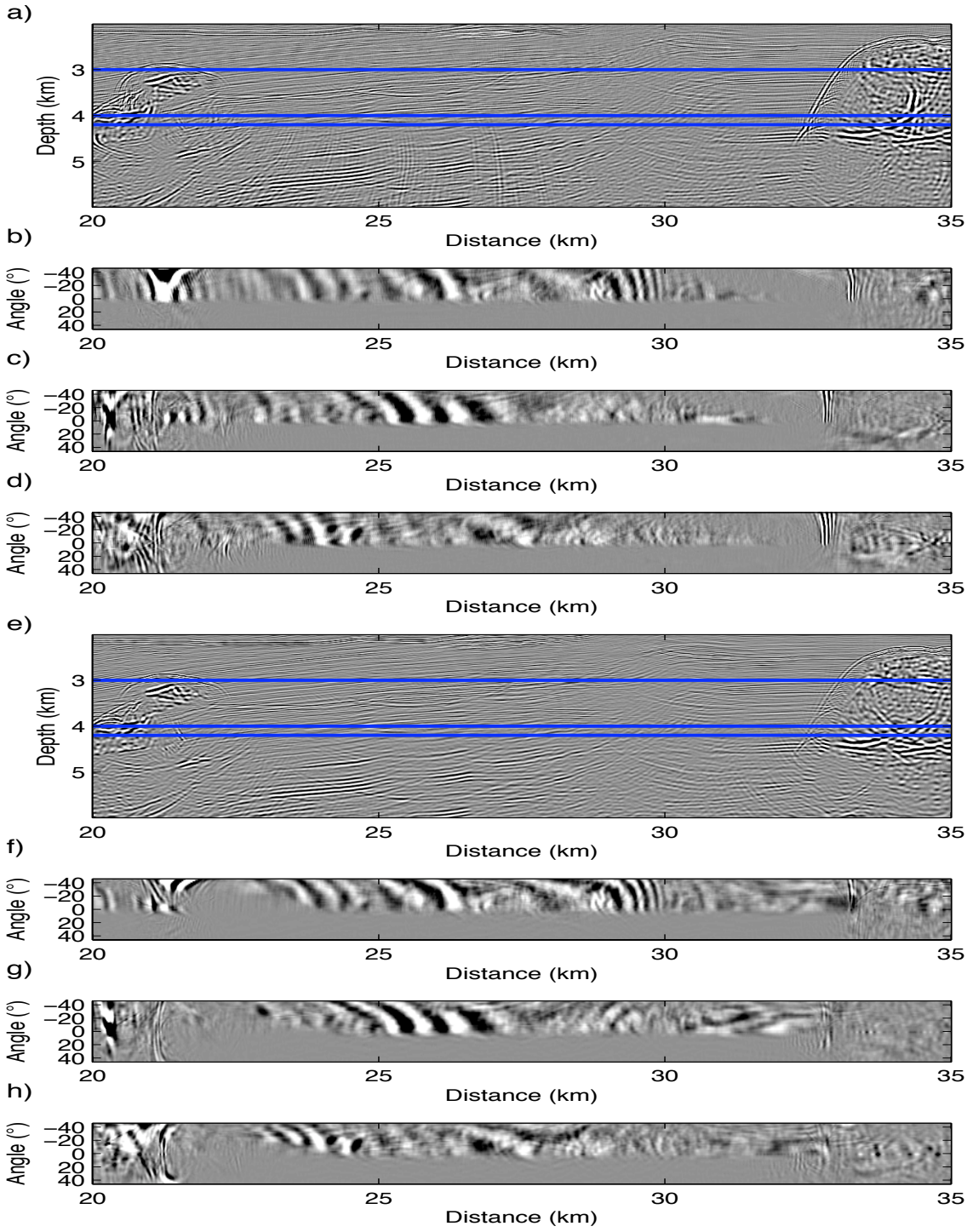

Figure 10: Horizontal elliptic and Cartesian ADCIGs slices using an incorrect migration velocity model. a) Elliptic coordinate image with three horizontal lines showing the locations of horizontal ADCIG gathers from top to bottom in panels b-d. e) Cartesian coordinate image with three horizontal lines showing the locations of horizontal ADCIG gathers from top to bottom in panels f-h.

systems well-suited to imaging steep geologic dips where 3D ADCIG volumes could be a good diagnostic tool for velocity analysis. **?** discusses how a judicious choice of 3D coordinate system depends greatly on the acquisition geometry and the desired migration geometry. For example, the migration geometries employed in shot-profile migration of wide-azimuth data sets are well-matched with 3D ellipsoidal meshes that enable high-angle and turning-wave propagation in all directions. Evaluating ADCIG image focussing in such a 3D coordinate geometry would then provide information on velocity model accuracy for steeply dipping reflectors - such as salt flanks. These somewhat speculative extensions, though, are beyond the scope of this paper and remain an active area of research.

CONCLUSIONS

I extend the Cartesian ADCIG theory to 2D generalized coordinate systems. The generalized ADCIG expressions related the reflection opening angle to differential traveltime operators and spatially varying weights derived from the non-Cartesian geometry. I show that these geometric expressions cancel out for coordinate systems satisfying the Cauchy-Riemann differentiability criteria, which include tilted Cartesian and elliptic meshes. The procedure for calculating ADCIGs in elliptic coordinates is very similar to that in Cartesian coordinates. I validate the approach by comparing analytically and numerically generated ADCIG volumes, and with tests on the BP synthetic data set. ADCIGs calculations are more robust where computed in elliptic coordinates than in Cartesian coordinate. I assert that this result is due to improved large-angle propagation and enhanced sensitivity to steep structural dips afforded by the coordinate transforms. Finally, the imaging advantages afforded by elliptic coordinates should improve the procedure of any migration velocity analysis approach that uses residual ADCIG curvature on steeply dipping reflectors to compute velocity model updates.

ACKNOWLEDGMENTS

I would like to thank Biondo Biondi, Alejandro Valenciano, Antoine Guitton and Brad Artman for helpful discussions, and BP for releasing the synthetic data used in the examples. I thank Tamas Nemeth, Samuel Gray, and an anonymous reviewer for helpful comments on the early stages of this manuscript. I acknowledge the sponsors of the SEP consortium for their continuing support.

REFERENCES

Lee, M. W. and S. Y. Suh, 1985, Optimization of one-way wave-equations (short note): Geophysics, **50**, 1634–1637.

APPENDIX A

ADCIG COORDINATE TRANSFORM

This appendix addresses how to express operators $\frac{\partial}{\partial x_3}$ and $\frac{\partial}{\partial h_{x_1}}$ in generalized coordinate systems to derive equation 10. I first assume that generalized coordinate systems are related to the Cartesian variables through a bijection (i.e., one-to-one mapping)

$$x_1 = f(\xi_1, \xi_3) \quad \text{and} \quad x_3 = g(\xi_1, \xi_3) \tag{A-1}$$

with a non-vanishing Jacobian of coordinate transformation, $J_{\boldsymbol{\xi}}$. The bijection between a generalized and Cartesian coordinate system allows us to rewrite the left-hand-sides of equations 7 as (**?**)

$$\frac{\partial t}{\partial x_1} = \frac{1}{J_{\boldsymbol{\xi}}} \frac{\partial (t, x_3)}{\partial (\xi_1, \xi_3)} \quad \text{and} \quad \frac{\partial t}{\partial x_3} = \frac{1}{J_{\boldsymbol{\xi}}} \frac{\partial (x_1, t)}{\partial (\xi_1, \xi_3)}. \tag{A-2}$$

Expanding the Jacobian notation leads to

$$\begin{bmatrix} \frac{\partial t}{\partial \xi_1}\frac{\partial x_3}{\partial \xi_3} - \frac{\partial t}{\partial \xi_3}\frac{\partial x_3}{\partial \xi_1} \\ \frac{\partial t}{\partial \xi_3}\frac{\partial x_1}{\partial \xi_1} - \frac{\partial t}{\partial \xi_1}\frac{\partial x_1}{\partial \xi_3} \end{bmatrix} = 2\, J_{\boldsymbol{\xi}}\, s \cos\gamma \begin{bmatrix} \sin\alpha \\ \cos\alpha \end{bmatrix}. \tag{A-3}$$

The right-hand-sides of equations A-3 are analogous to those derived by **?**. Cross-multiplying the expressions by factors $\frac{\partial x_1}{\partial \xi_3}$ and $\frac{\partial x_3}{\partial \xi_3}$

$$\begin{bmatrix} \frac{\partial x_1}{\partial \xi_3}\left(\frac{\partial t}{\partial \xi_1}\frac{\partial x_3}{\partial \xi_3} - \frac{\partial t}{\partial \xi_3}\frac{\partial x_3}{\partial \xi_1}\right) \\ \frac{\partial x_3}{\partial \xi_3}\left(\frac{\partial t}{\partial \xi_3}\frac{\partial x_1}{\partial \xi_1} - \frac{\partial t}{\partial \xi_1}\frac{\partial x_1}{\partial \xi_3}\right) \end{bmatrix} = 2\, J_{\boldsymbol{\xi}}\, s \cos\gamma \begin{bmatrix} \frac{\partial x_1}{\partial \xi_3}\sin\alpha \\ \frac{\partial x_3}{\partial \xi_3}\cos\alpha \end{bmatrix} \tag{A-4}$$

and adding the two expressions results in

$$\frac{\partial t}{\partial \xi_3}\left(\frac{\partial x_3}{\partial \xi_3}\frac{\partial x_1}{\partial \xi_1} - \frac{\partial x_1}{\partial \xi_3}\frac{\partial x_3}{\partial \xi_1}\right) = 2\, J_{\boldsymbol{\xi}}\, s \cos\gamma \left(\frac{\partial x_1}{\partial \xi_3}\sin\alpha + \frac{\partial x_3}{\partial \xi_3}\cos\alpha\right). \tag{A-5}$$

A similar argument can be used to construct the equations for the subsurface-offset axis. The bijection between the generalized coordinate and Cartesian subsurface-offset axes allows for the left-hand-side of equations 7 to be rewritten as

$$\frac{\partial t}{\partial h_{x_1}} = \frac{1}{J_{\boldsymbol{h}}} \frac{\partial (t, h_{x_3})}{\partial (h_{\xi_1}, h_{\xi_3})} \quad \text{and} \quad \frac{\partial t}{\partial h_{x_3}} = \frac{1}{J_{\boldsymbol{h}}} \frac{\partial (h_{x_1}, t)}{\partial (h_{\xi_1}, h_{\xi_3})}, \tag{A-6}$$

where $J_{\boldsymbol{h}}$ is the subsurface-offset Jacobian of transformation. Expanding the Jacobian notation leads to

$$\begin{bmatrix} \frac{\partial t}{\partial h_{\xi_1}}\frac{\partial h_{x_3}}{\partial h_{\xi_3}} - \frac{\partial t}{\partial h_{\xi_3}}\frac{\partial h_{x_3}}{\partial h_{\xi_1}} \\ \frac{\partial t}{\partial h_{\xi_3}}\frac{\partial h_{x_1}}{\partial h_{\xi_1}} - \frac{\partial t}{\partial h_{\xi_1}}\frac{\partial h_{x_1}}{\partial h_{\xi_3}} \end{bmatrix} = 2\, J_{\boldsymbol{h}}\, s \sin\gamma \begin{bmatrix} \cos\alpha \\ \sin\alpha \end{bmatrix}. \tag{A-7}$$

The right-hand-side of equations A-7 are again analogous to those given by **?**. Cross-multiplying the expressions by factors $\frac{\partial h_{x_1}}{\partial h_{\xi_1}}$ and $\frac{\partial h_{x_3}}{\partial h_{\xi_1}}$

$$\begin{bmatrix} \frac{\partial h_{x_1}}{\partial h_{\xi_1}} \left(\frac{\partial t}{\partial h_{\xi_1}} \frac{\partial h_{x_3}}{\partial h_{\xi_3}} - \frac{\partial t}{\partial h_{\xi_3}} \frac{\partial h_{x_3}}{\partial h_{\xi_1}} \right) \\ \frac{\partial h_{x_3}}{\partial h_{\xi_1}} \left(\frac{\partial t}{\partial h_{\xi_3}} \frac{\partial h_{x_1}}{\partial h_{\xi_1}} - \frac{\partial t}{\partial h_{\xi_1}} \frac{\partial h_{x_1}}{\partial h_{\xi_3}} \right) \end{bmatrix} = 2\, J_{\boldsymbol{h}}\, s \sin\gamma \begin{bmatrix} \frac{\partial h_{x_1}}{\partial h_{\xi_1}} \cos\alpha \\ \frac{\partial h_{x_3}}{\partial h_{\xi_1}} \sin\alpha \end{bmatrix}, \tag{A-8}$$

and subtracting the two expressions above yields

$$\frac{\partial t}{\partial h_{\xi_1}} \left(\frac{\partial h_{x_1}}{\partial h_{\xi_1}} \frac{\partial h_{x_3}}{\partial h_{\xi_3}} - \frac{\partial h_{x_1}}{\partial h_{\xi_3}} \frac{\partial h_{x_3}}{\partial h_{\xi_1}} \right) = 2\, J_{\boldsymbol{h}}\, s \sin\gamma \left(\frac{\partial h_{x_1}}{\partial h_{\xi_1}} \cos\alpha - \frac{\partial h_{x_3}}{\partial h_{\xi_1}} \sin\alpha \right). \tag{A-9}$$

An expression for ADCIGs can be obtained by dividing equation A-9 by equation A-5

$$\frac{\frac{\partial t}{\partial h_{\xi_1}}}{\frac{\partial t}{\partial \xi_3}} \frac{\left(\frac{\partial h_{x_1}}{\partial h_{\xi_1}} \frac{\partial h_{x_3}}{\partial h_{\xi_3}} - \frac{\partial h_{x_1}}{\partial h_{\xi_3}} \frac{\partial h_{x_3}}{\partial h_{\xi_1}} \right)}{\left(\frac{\partial x_3}{\partial \xi_3} \frac{\partial x_1}{\partial \xi_1} - \frac{\partial x_1}{\partial \xi_3} \frac{\partial x_3}{\partial \xi_1} \right)} = \tan\gamma\, \frac{J_{\boldsymbol{h}}}{J_{\boldsymbol{\xi}}} \frac{\left(\frac{\partial h_{x_1}}{\partial h_{\xi_1}} \cos\alpha - \frac{\partial h_{x_3}}{\partial h_{\xi_1}} \sin\alpha \right)}{\left(\frac{\partial x_3}{\partial \xi_3} \cos\alpha + \frac{\partial x_1}{\partial \xi_3} \sin\alpha \right)}. \tag{A-10}$$

One question arising from the geometric factors in equation A-10 is what do the terms $\frac{\partial h_{x_1}}{\partial h_{\xi_1}}$, $\frac{\partial h_{x_3}}{\partial h_{\xi_1}}$, $\frac{\partial h_{x_1}}{\partial h_{\xi_3}}$ and $\frac{\partial h_{x_3}}{\partial h_{\xi_3}}$ represent? I assume that the subsurface offset axes are generated by uniform wavefield shifting such that the following equations are valid:

$$\begin{bmatrix} h_{x_1} \\ h_{x_3} \\ h_{\xi_1} \\ h_{\xi_1} \end{bmatrix} = \begin{bmatrix} x_1 \\ x_3 \\ \xi_1 \\ \xi_3 \end{bmatrix} \quad \text{such that} \quad \begin{bmatrix} \frac{\partial h_{x_1}}{\partial h_{\xi_1}} \\ \frac{\partial h_{x_3}}{\partial h_{\xi_1}} \\ \frac{\partial h_{x_1}}{\partial h_{\xi_3}} \\ \frac{\partial h_{x_3}}{\partial h_{\xi_3}} \end{bmatrix} = \begin{bmatrix} \frac{\partial x_1}{\partial \xi_1} \\ \frac{\partial x_3}{\partial \xi_1} \\ \frac{\partial x_1}{\partial \xi_3} \\ \frac{\partial x_3}{\partial \xi_3} \end{bmatrix}. \tag{A-11}$$

If the subsurface offset axes were generated by anything other than uniform shifting (e.g. $h_{x_1} = x_1^2$), then the assumptions behind equations A-11 would not be honored.

Using these identities in equation A-5 reduces equation A-10 to

$$-\left. \frac{\partial \xi_3}{\partial h_{\xi_1}} \right|_{\xi_1, t} = \frac{\partial t}{\partial h_{\xi_1}} \Big/ \frac{\partial t}{\partial \xi_3} = \tan\gamma\, \frac{\left(\frac{\partial x_1}{\partial \xi_1} \cos\alpha - \frac{\partial x_3}{\partial \xi_1} \sin\alpha \right)}{\left(\frac{\partial x_3}{\partial \xi_3} \cos\alpha + \frac{\partial x_1}{\partial \xi_3} \sin\alpha \right)}, \tag{A-12}$$

where the two Jacobian transformations are equivalent (i.e. $J_{\boldsymbol{\xi}} = J_{\boldsymbol{h}}$). This completes the derivation of equation 10.